SCIENCE CHINA
Earth Sciences

• RESEARCH PAPER •

August 2017 Vol.60 No.8: 1495–1506
doi: 10.1007/s11430-016-9052-1

Thermospheric mass density derived from CHAMP satellite precise orbit determination data based on energy balance method

LI RuoXi[1], LEI JiuHou[1*], WANG XiJing[2], DOU XianKang[1] & JIN ShuangGen[3]

[1] *School of Earth and Space Science, University of Science and Technology China, Hefei 230026, China;*
[2] *Key Laboratory for Fault Diagnosis and Maintenance of Spacecraft In-orbit, Xi'an 710043, China;*
[3] *Shanghai Astronomical Observatory, Chinese Academy of Sciences, Shanghai 200030, China*

Received March 4, 2017; accepted May 10, 2017; published online July 13, 2017

Abstract In this article, the energy balance method is used to retrieve thermospheric mass density from CHAMP satellite precise orbit determination (POD) data during 2007–2009. The retrieved thermospheric mass densities are compared with those from accelerometer data and an empirical model. The main conclusions are as follows: (1) Thermospheric mass density can be retrieved from POD data by the energy balance and semi-major axis decay methods, whose results are consistent. (2) The accuracy of the retrieved densities depends on the integration time period, and the optimal period for CHAMP density retrieval from POD data is about 20 minutes. (3) The energy balance method can be used to calibrate accelerometer data. (4) The accuracy of retrieving thermospheric density from POD data varies with satellite altitude and local time.

Keywords Thermospheric mass density, Satellite orbit, Semi-major axis, Energy balance, Accelerometer

Citation: Li R X, Lei J H, Wang X J, Dou X K, Jin S G. 2017. Thermospheric mass density derived from CHAMP satellite precise orbit determination data based on energy balance method. Science China Earth Sciences, 60: 1495–1506, doi: 10.1007/s11430-016-9052-1

1. Introduction

Thermospheric mass density has a major impact on spacecraft control and life (Emmert, 2015). Empirical models such as DTM (Berger et al., 1998) and MSIS (Hedin, 1987) are widely used to calculate the atmospheric perturbation force on a low Earth orbit satellite. In general, the average error of thermospheric mass density calculated by empirical models is about 15–20% (Marcos, 1990), and the error increases during storm periods (Emmert, 2015; Bowman et al., 2008). This is of great importance to observing, retrieving and predicting thermospheric mass density.

Picone et al. (2005) retrieved thermospheric mass density from two line element (TLE) data. However, temporal resolution of the TLE retrieved density is poor because of low cadency of the TLE tracking data. With the launch of CHAMP (Reigber et al., 2002), GRACE (Tapley et al., 2004) and other satellites carrying high-precision accelerometers, scientists (Bruinsma and Biancale, 2003; Sutton et al., 2007; Doornbos, 2012; Li et al., 2016) have obtained thermospheric mass density with high spatial and temporal resolution from accelerometer data. Thermospheric mass density retrieved from accelerometer data has been widely used to study thermospheric response to geomagnetic storms and other space weather events (e.g., Lei et al., 2011a, 2012). The accelerometer data must be calibrated to derive thermospheric mass density. Sutton et al. (2007) and Doornbos (2012) estimated calibration factors directly by the method of orbit determination. Xiong et al. (2011) simplified the method of calculating calibration factors from orbit determination using CHAMP Rapid Science Orbit (RSO) data as observations. The observed acceleration was calibrated as a non-conservative force to estimate only the calibration factors. However, such orbit determination is still a complicated

* Corresponding author (email: leijh@ustc.edu.cn)

procedure. Using the energy balance method, Xu and Yang (2004) estimated the calibration factors with high operational efficiency, based on the obtained high-precision earth gravity field. This is an effective means to retrieve thermospheric mass density from accelerometer data, but only a few satellites carry high-precision accelerometers. Without using accelerometer data, Calabia and Jin (2016) retrieved thermospheric mass density from GRACE satellite POD data, but the accuracy of this method relies heavily on the high frequency of GRACE satellite POD data. Sang et al. (2012) also retrieved thermospheric mass density from CHAMP POD data with high spatial and temporal resolution. However, they only presented a few days' results and there was no statistical analysis or validation for a long period. Further, they did not take into account the impact of time-varying satellite attitude and drag coefficient.

This paper presents a new method to retrieve thermospheric mass density based on energy balance. Without numerical integration, this method has high computational efficiency, and the retrieval process can be used to calibrate CHAMP accelerometer data. Mass densities retrieved from POD data are compared with those from accelerometer data and the MSIS00 model (Picone et al., 2002) to validate the retrieval method.

2. Methodology

In this section, satellite POD data are used to retrieve thermospheric mass density using both the semi-major axis decay and energy balance methods. Density is also retrieved from satellite accelerometer data.

2.1 Thermospheric mass density retrieved from semi-major axis decay method

A satellite semi-major axis decays because of atmospheric drag and, given this, atmospheric mass density can be retrieved from the decay rate. According to the satellite orbit perturbation equation (Liu, 1992), the variation rate of the semi-major axis from atmospheric drag is

$$\frac{\mathrm{d}a}{\mathrm{d}t} = \frac{2}{n\sqrt{1-e^2}}(1+2e\cos f+e^2)^{1/2}U, \tag{1}$$

where a, e, f and n stand for the semi-major axis, eccentricity, true anomaly and mean motion, respectively. U is the tangential perturbation caused by atmospheric drag:

$$U = \frac{1}{2}\frac{C_D A}{m}\rho v_r^2, \tag{2}$$

here, C_D is the drag coefficient, A the effective cross-sectional area, m the satellite mass, ρ atmospheric density, and v_r the velocity of relative motion between satellite and atmosphere. The atmosphere and earth are assumed to have the same rotation speed. Thus, according to eqs. (1) and (2), the atmospheric density can be expressed as

$$\rho = -\frac{\mathrm{d}a}{\mathrm{d}t}\Bigg/\left(\frac{C_D A}{m}v_r^2\frac{(1+2e\cos f+e^2)^{1/2}}{n\sqrt{1-e^2}}\right), \tag{3}$$

RSO data of the CHAMP satellite were used as POD data in this study. CHAMP is a German satellite for geoscientific and atmospheric research and applications (Reigber et al., 2002). It was launched into a near-circular orbit at 454 km with 87° inclination on July 15, 2000. Level3 RSO data were obtained using the method of GPS orbit determination that gives the satellite state vector (location and speed) every 30 seconds (König et al., 2001). Orbit determination precision was ~20 cm at the beginning of the mission and increased to 5 cm during later periods (Michalak et al., 2003). The satellite state vector at a specific time t_0 is taken as the initial state vector. The state vector at t_1 can be calculated using numerical integration, considering all the perturbation forces except atmospheric drag. Then, the instantaneous semi-major axis is obtained as $a_{\mathrm{no\_drag}}$. The real instantaneous semi-major axis, denoted a_{real}, can be calculated using the orbit state vector at t_1 from RSO data. The decay rate of the semi-major axis owing to atmospheric drag $\left.\frac{\mathrm{d}a}{\mathrm{d}t}\right|_{\mathrm{drag}}$ is expressed as follows (Sang et al., 2012):

$$\left.\frac{\mathrm{d}a}{\mathrm{d}t}\right|_{\mathrm{drag}} = \frac{a_{\mathrm{real}}-a_{\mathrm{no\_drag}}}{\Delta t}, \tag{4}$$

where $t_1=t_0+\Delta t$. a, e, f and n can be calculated using RSO data. The thermospheric mass density can be obtained from eqs. (3) and (4):

$$\rho = \frac{\left.\frac{\mathrm{d}a}{\mathrm{d}t}\right|_{\mathrm{drag}}}{\left(\frac{C_D A}{m}v_r^2\frac{(1+2e\cos f+e^2)^{1/2}}{n\sqrt{1-e^2}}\right)}. \tag{5}$$

Then, we calculated the transfer error from orbit determination as $\Delta a=a_{\mathrm{real}}-a_{\mathrm{no\_drag}}$ in order to analyze the impact of orbit determination error on thermospheric mass density retrieval. The Vis-viva law is

$$a = \left(\frac{2}{r}-\frac{v^2}{\mu}\right)^{-1}. \tag{6}$$

According to the measured error transfer equation, we have

$$\delta_a^2 = \frac{4a^4}{r^4}\delta_r^2 + \frac{4v^2a^4}{\mu^2}\delta_v^2. \tag{7}$$

We have $a\approx r=6750000$ m, $v=7500\,\mathrm{m\,s^{-1}}$, $\mu=3.986\times10^{14}\,\mathrm{m^3\,s^{-2}}$, and the measurement error of position and velocity is $\delta_r=0.05$ m and $\delta_v=0.00005\,\mathrm{m\,s^{-1}}$, respectively. measurement error of the semi-major axis becomes $\delta_a^2\approx 4\delta_r^2+3\times10^{-6}\delta_v^2\approx 0.13$ m.

If $a_{\mathrm{no\_drag}}$ and a_{real} have the same uncertainty, the uncertainty of Δa can be written as

$$\delta_{\Delta a} = \sqrt{2}\,\delta_a = 0.18\ \mathrm{m}. \tag{8}$$

The uncertainty of Δa from orbit determination error is as large as 0.18 m, so an appropriate time interval Δt must be carefully chosen to ensure that $\Delta a = a_{\text{real}} - a_{\text{no\_drag}}$ is > 0.18 m during the retrieval time interval.

2.2 Thermospheric mass density derived from energy balance method

Satellite total energy decreases because of atmospheric drag, and atmospheric mass density can be derived from that decrease. Based on the 100-order EGM2008 gravity field model (Pavlis et al., 2008), solid tide model obtained by correcting gravity field coefficients according to IERS2010 (Petit and Luzum, 2010), ocean tide model of Li (1995), third body gravitational field model according to E405 ephemeris, atmospheric drag, and solar pressure, the total energy for the satellite in orbit can be expressed as

$$E_0 = \frac{1}{2}|v|^2 - V_{\text{SUN}} - V_{\text{MOON}} - \frac{1}{2}\omega^2(x^2 - y^2) - V - E_n. \tag{9}$$

On the right side of the equation, the $\frac{1}{2}|v|^2$ is kinetic energy of the satellite; the V_{SUN} and V_{MOON} represent the gravitational potential of the sun and moon, respectively; the $\frac{1}{2}\omega^2(x^2 - y^2)$ represents rotation potential energy (Jekeli, 1999); the V stands for the earth's gravity field; the E_n is work of the non-conservative force. The latter can be expressed as the integration of non-conservative force along the satellite path in the inertial system:

$$E_n = \int \boldsymbol{a} \cdot \boldsymbol{v} \mathrm{d}t, \tag{10}$$

where $\boldsymbol{a}$ stands for the acceleration of non conservative forces and $\boldsymbol{v}$ is satellite speed. At a specific time t_0, total mechanical energy of the satellite can be calculated. After time interval Δt, that energy can also be calculated at t_1, where $t_1 = t_0 + \Delta t$. The total mechanical energy decreases from t_0 to t_1 under the influence of atmospheric drag and solar pressure, so we have

$$\int \boldsymbol{a}_{\text{drag}} \cdot \boldsymbol{v} \mathrm{d}t + \int \boldsymbol{a}_{\text{solarpress}} \cdot \boldsymbol{v} \mathrm{d}t = \left(\frac{1}{2}|\boldsymbol{v}|^2 - V_{\text{SUN}} - V_{\text{MOON}} - \frac{1}{2}\omega^2(x^2 - y^2) - V - E_0 \right) \Big|_{t_0}^{t_1}, \tag{11}$$

here, $\boldsymbol{a}_{\text{drag}}$ and $\boldsymbol{a}_{\text{solarpress}}$ designate atmospheric drag and solar pressure.

Because the direction of atmospheric drag is opposite satellite motion, the work of atmospheric drag can be approximated as

$$\int \boldsymbol{a}_{\text{drag}} \cdot \boldsymbol{v} \mathrm{d}t = a_{\text{drag}} |\boldsymbol{v}| \Delta t. \tag{12}$$

From eqs. (2) and (11), the average atmospheric density along the satellite path during Δt is

$$\rho_{\text{drag}} = \left(\frac{1}{2}|\boldsymbol{v}|^2 - V_{\text{SUN}} - V_{\text{MOON}} - \frac{1}{2}\omega^2(x^2 - y^2) - V - E_0 - \int \boldsymbol{a}_{\text{solarpress}} \cdot \boldsymbol{v} \mathrm{d}t \right) \Big|_{t_0}^{t_1} \Big/ \left(|\boldsymbol{v}| \Delta t \frac{1}{2} \frac{C_D A}{m} v_r^2 \right). \tag{13}$$

Next, we address the relationship between thermospheric densities from the semi-major axis decay and energy decay methods. In the polar coordinate system, the variation rate of the semi-major axis from atmospheric drag can be written as (Liu, 1992):

$$-\frac{GM}{a^2}\frac{\mathrm{d}a}{\mathrm{d}t} = -2\dot{\boldsymbol{r}} \cdot \boldsymbol{S} - 2r\dot{\boldsymbol{\theta}} \cdot \boldsymbol{T}, \tag{14}$$

where r, $\dot{\boldsymbol{r}}$, $\boldsymbol{\theta}$ and $\dot{\boldsymbol{\theta}}$ stand for position, velocity, angle and angular velocity in the polar coordinate system, respectively. Neglecting the radial component, eq. (14) is consistent with eq. (1). Rewriting the left side of eq. (14) in the form of a total differential and considering that $\dot{\boldsymbol{r}} \cdot \boldsymbol{S} + r\dot{\boldsymbol{\theta}} \cdot \boldsymbol{T} = \boldsymbol{F} \cdot \boldsymbol{V}$, we have

$$\mathrm{d}\left(\frac{GM}{2a}\right) = -\boldsymbol{F} \cdot \boldsymbol{V} \mathrm{d}t. \tag{15}$$

According to the Vis-viva law, $\frac{GM}{2a} = \frac{GM}{r} - \frac{1}{2}v^2 = E_0$. The left side of eq. (15) represents the change of energy, and the right side is converted into work of the non-conservative force. Therefore, the mathematical principles of the two methods are consistent. The major difference is that numerical integration is needed in the semi-major axis decay method, which may introduce calculation error. In the present study, the time interval for orbit extrapolation was short, so the error from numerical integration is small.

2.3 Thermospheric mass density from accelerometer data

The CHAMP satellite carries a high-precision accelerometer, with great accuracy along the direction of satellite motion. Measurement accuracy can be as great as 3×10^{-9} m s^{-2} (Flury et al., 2008). The accelerometer data, which are released by German Research Centre for Geosciences (GFZ), are part of the Level3 Orbit/Gravity data. The accelerometer data document includes initial acceleration measurement a_0, Lorentz force correction a_L, radial component correction a_{tm}, satellite attitude, and also shows thruster activation times (Förste et al., 2002). The observed acceleration is obtained by correcting a_0 with Lorentz force correction and radial component correction:

$$a_{\text{observe}} = a_0 + a_L + a_{tm}. \tag{16}$$

The observed data from the accelerometer should be further calibrated, and the calibration equation is as follows (Bruinsma et al., 2004).

$$a_{IFX} = Scale \times a_{\text{observe}} + Bias, \tag{17}$$

where *Scale* and *Bias* are calibration factors and a_{IFX} is acceleration after calibration in the instrument coordinate system. a_{IFX} must be transformed from the instrument coordinate system to the satellite coordinate system and then to the inertial coordinate system (Lühr et al., 2001). The coordinate transformation equation becomes

$$a_{INF} = R_{IFX\to INF} a_{IFX}, \tag{18}$$

where $R_{IFX\to INF}$ stands for the coordinate transformation matrix from the instrument coordinate system to the inertial coordinate system. Finally, the atmospheric density is calculated according to eq. (2):

$$\rho = a_{INF} \Big/ \left(\frac{1}{2} \frac{C_D A}{m} v_r^2 \right). \tag{19}$$

Acceleration measured by an accelerometer is instantaneous, whereas equivalent acceleration calculated from POD data is mean acceleration during the time interval, so its accuracy is less than that from an accelerometer. The accelerometer data calibration method and results are presented in Section 2.2.

3. The calculation of effective cross-section area and drag coefficient, and calibration of accelerometer data

3.1 Effective cross-sectional area and drag coefficient

The drag coefficient is an important parameter in retrieving atmospheric density, according to eq. (5). According to Sentman (1961), the product of that coefficient and the effective cross-sectional area of each surface panel of the CHAMP satellite can be expressed as

$$(C_D \cdot A) = \left(\frac{P}{\sqrt{\pi}} + \gamma Q Z + \frac{\gamma}{2} \frac{v_{out}}{v_r} (\gamma \sqrt{\pi} Z + P) \right) \cdot A, \tag{20}$$

where

$$\begin{aligned} &G = \frac{1}{2S^2}, P = \frac{1}{S} \exp(-\gamma^2 S^2), \\ &Q = 1 + G, Z = 1 + erf(\gamma S), \end{aligned} \tag{21}$$

γ stands for the angle between the normal direction of each satellite surface panel and the direction of $-\boldsymbol{v}_r$ in the satellite coordinate system:

$$\gamma = -\boldsymbol{u}_D \cdot \boldsymbol{u}_N, \tag{22}$$

where $\boldsymbol{u}_N$ and $\boldsymbol{u}_D$ represent the unit vector of $\boldsymbol{v}_r$ and unit normal vector of each satellite surface panel, respectively.

S is the ratio between relative speed of the satellite with respect to a rotating atmosphere and the most probable thermal speed of atmospheric molecules:

$$S = \frac{v_r}{\sqrt{\frac{2RT}{m_a}}}, \tag{23}$$

where T and m_a symbolize local temperature and relative molecular mass of the atmosphere estimated by MSIS00, respectively.

$$T_{\text{in}} = \frac{m_a v_r^2}{3R}, \tag{24}$$

where T_{in} stands for the kinetic temperature of the incident gas atoms and R is a thermodynamic constant.

v_{out} denotes the velocity of re-admitted gas atoms:

$$v_{\text{out}} = v_r \sqrt{\frac{2}{3}\left[1 + \alpha_E \left(\frac{T_{\text{wall}}}{T_{\text{in}}} - 1 \right)\right]}, \tag{25}$$

where T_{wall} represents satellite surface temperature, which is considered to be as low as 300 K. α_E is related to the ratio between the relative molecular mass of the atmosphere and that of satellite materials, which can be expressed as

$$\alpha_E = \frac{2\mu}{(1+\mu)^2}, \tag{26}$$

where μ represents the ratio between the relative molecular mass of the atmosphere and that of satellite material. It is assumed that the satellite material is mainly oxygen silicon and that the main component of the atmosphere is oxygen atoms. α_E is then set to 0.93 (Doornbos et al., 2009).

The drag coefficient and effective cross-sectional area vary with time because of the change of atmospheric temperature and satellite attitude. Figure 1 shows variation of the products of drag coefficients and effective cross-sectional areas of CHAMP on day 32 of 2009. With the maximum value ~2.35 and the minimum ~1.95, the relative variation can be as large as 20%.

3.2 Accelerometer data calibration

As mentioned in Section 1.3, accelerometer data have to be calibrated before retrieving thermospheric density. Bias and scale factors can be calculated according to eq. (17). We used the energy balance method to calibrate the accelerometer data. Atmospheric drag is considered the most important non-conservative force along the direction of satellite motion. Replacing non-conservative force in eq. (11) with atmospheric drag shown in eq. (17), we have (Xu and Yang, 2004):

$$\begin{aligned} &\int \left(Scale \times \boldsymbol{a}_{\text{observe}} + Bias \right) \cdot |\boldsymbol{v}| \mathrm{d}t \\ &= \left(\frac{1}{2}|\boldsymbol{v}|^2 - V_{\text{SUN}} - V_{\text{MOON}} \right. \\ &\quad \left. - \frac{1}{2}\omega^2 (x^2 - y^2) - V - E_0 \right) \Big|_{t_0}^{t_1}, \end{aligned} \tag{27}$$

here, $|v|$ stands for the absolute value of satellite velocity vector. We change the form of eq. (27) to

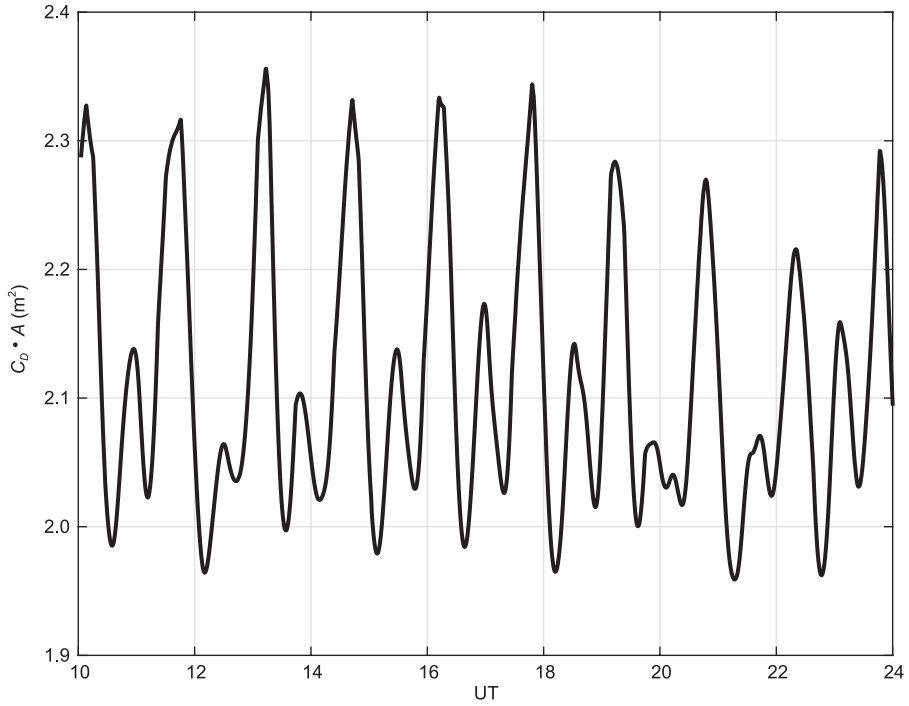

Figure 1 Product of drag coefficient and effective cross-sectional area of CHAMP satellite on day 32, 2009.

$$\begin{aligned} &Scale \times \boldsymbol{a}_{\text{observe}} + Bias \\ &= \left(\frac{1}{2}|\boldsymbol{v}|^2 - V_{\text{SUN}} - V_{\text{MOON}} \right. \\ &\left. -\frac{1}{2}\omega^2(x^2 - y^2) - V - E_0\right)\Big|_{t_0}^{t_1} \Big/ \int |\boldsymbol{v}|\Delta t. \end{aligned} \tag{28}$$

For the ith observed data, the right side of eq. (28) is denoted A^i. eq. (28) is then transformed into

$$Scale \times a^{i}_{\text{observe}} + Bias = A^i. \tag{29}$$

Figure 2 shows daily bias factors from 2007 to 2009 using the least squares fitting method. The scale factor was generally unchanged, and was set to be the priori value of 0.8333 (Förste et al., 2002). The thermospheric density was then retrieved from the calibrated acceleration according to eq. (19). As shown in Figure 3, thermospheric densities from accelerometer data show good agreement with those from the University of Colorado team (Sutton et al., 2007). The correlation coefficient was as large as 0.99. This indicates that it is convenient and efficient to calibrate accelerometer data using the energy balance method.

4. Results and discussion

Figure 4 shows thermospheric mass densities derived from POD data using the semi-major axis decay and energy balance methods on day 32 of 2009. Δt was set as 150 s. It is clear that POD-based thermospheric densities from the two methods are in good agreement, and are also consistent with those derived from accelerometer data, except for high-frequency oscillations in the POD-based thermospheric densities. Those are mainly associated with orbit determination error. The computation time for density retrieval from the energy balance method is less than that from the semi-major axis decay method, by a factor of ~10. Therefore, thermospheric densities derived from POD data based on the energy decay method were used in the following comparison.

Figure 5 shows thermospheric densities retrieved from POD data and those from accelerometer data on February 4–5, 2009, February 24, 2009, and March 21, 2009. The reason for choosing these days is that Sang et al. (2012) also compared atmospheric densities obtained from POD data with those from accelerometer data during these days. Again, thermospheric densities from these two methods are in good agreement. This is consistent with the results of Sang et al. (2012). Note that the data gaps of the retrieved densities from POD data and accelerometer data are associated with satellite attitude adjustment.

Thermospheric densities from both the semi-major axis decay and energy balance methods are generally in agreement with those from accelerometer data, but during nighttime there were evident discrepancies. This is probably associated with low atmospheric density at night, which corresponds to less change in both the semi-major axis and energy and introduces large errors in density retrieval. When Δt was set to 20 minutes, rapid fluctuations in the POD thermospheric densities tended to disappear. For a longer Δt, the densities retrieved from POD data in Figure 6 show better agreement

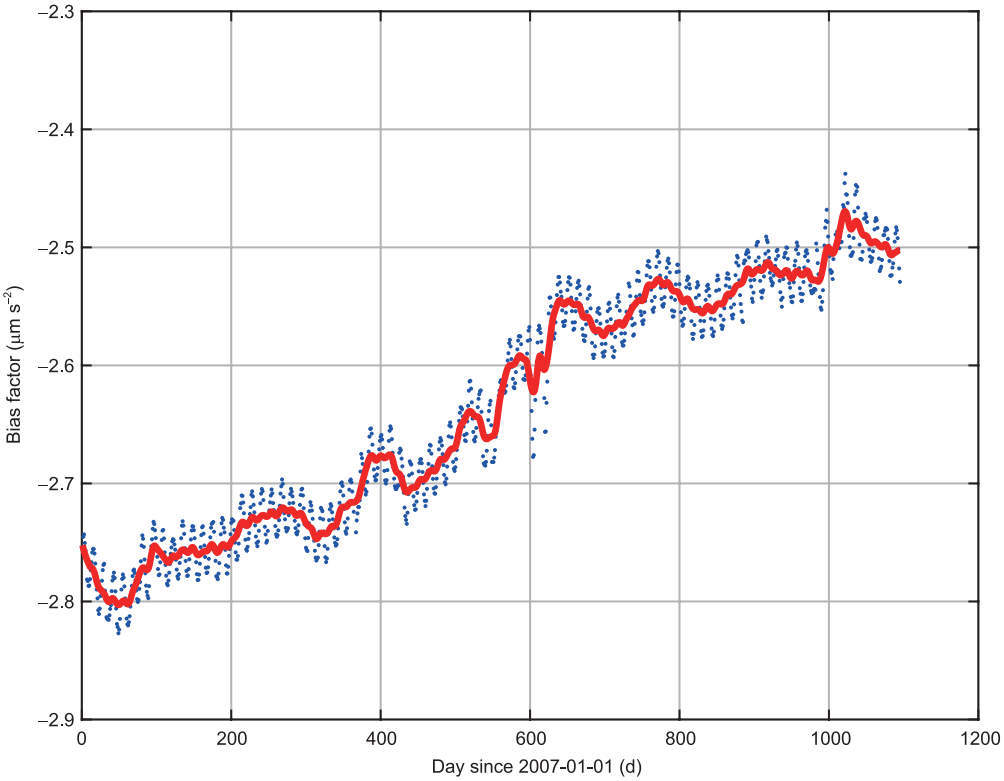

Figure 2 Bias factors from 2007 to 2009 with constant scale factor. Red line represents 20-day moving average.

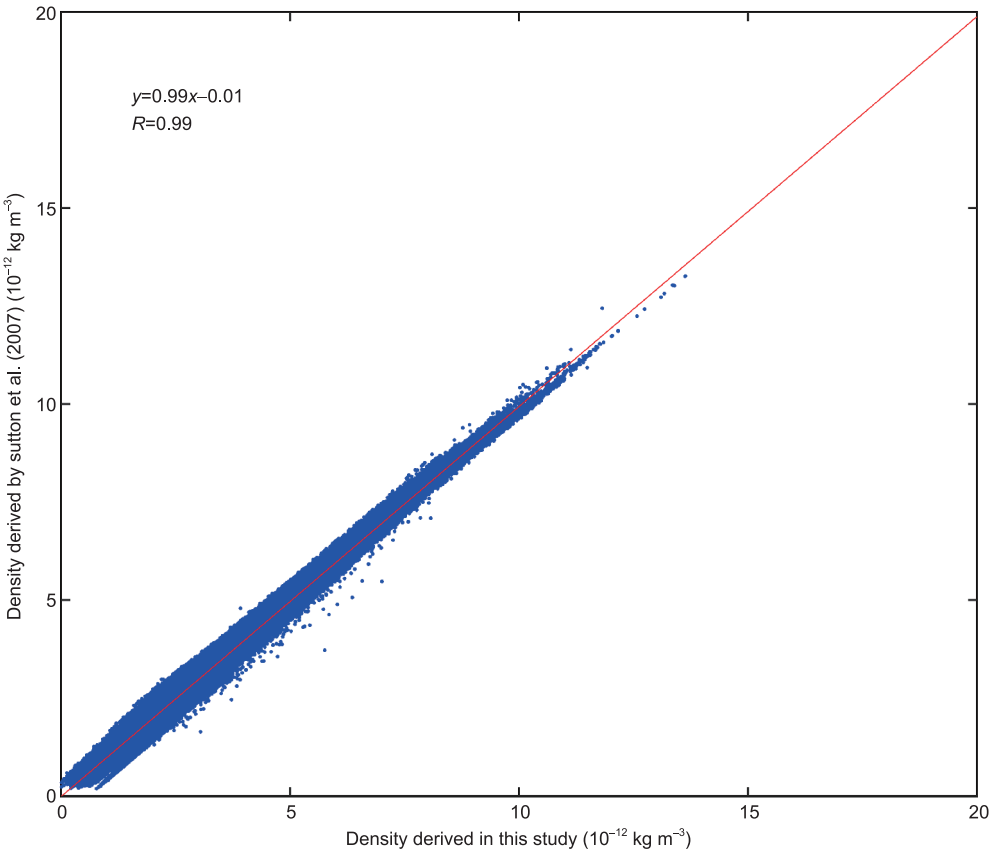

Figure 3 Comparison between densities retrieved from accelerometer data and those of Sutton et al. (2007).

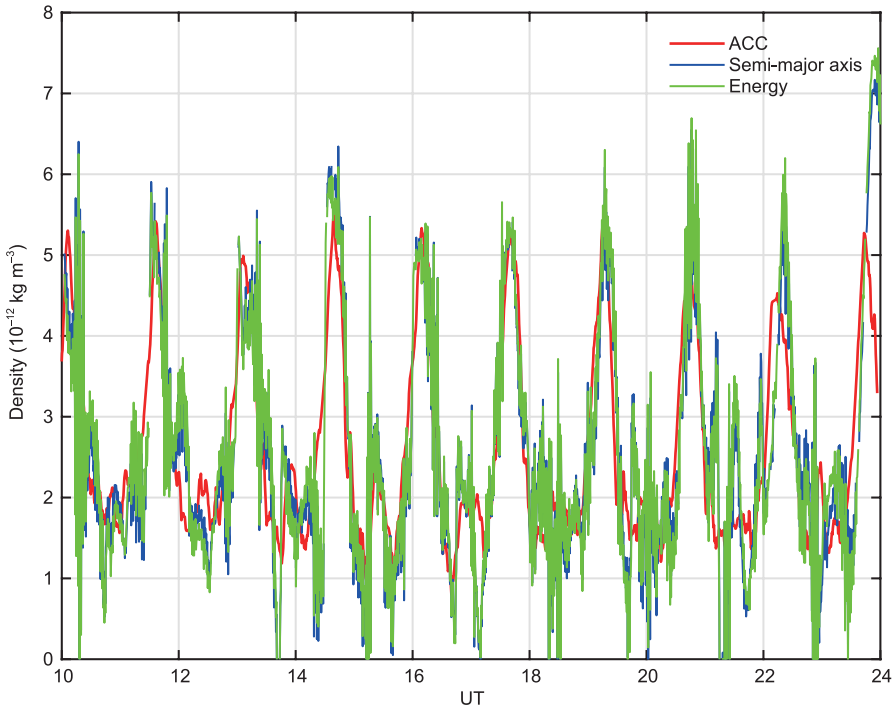

Figure 4 Comparison of thermospheric densities derived from semi-major axis decay method (blue), energy balance method (green), and accelerometer data (red) on day 32, 2009. Time interval was set to 150 s.

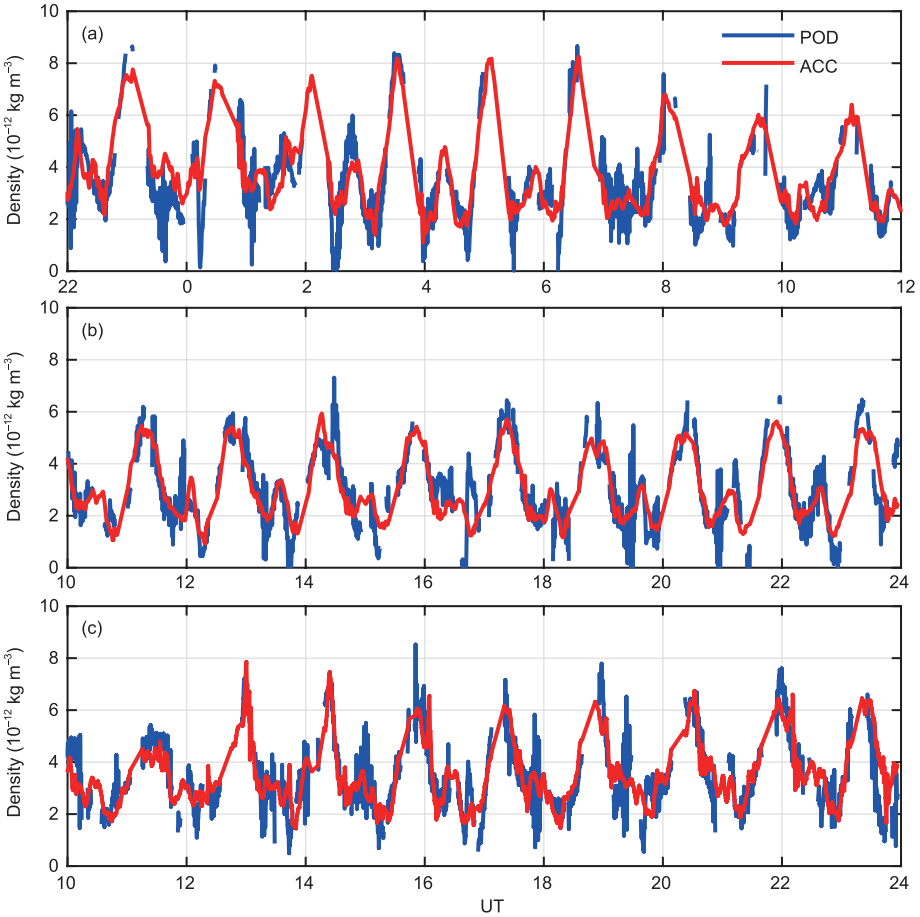

Figure 5 Comparison of densities derived from accelerometer data and POD data on February 4–5, 2009 (a), February 24, 2009 (b), and March 21, 2009 (c).

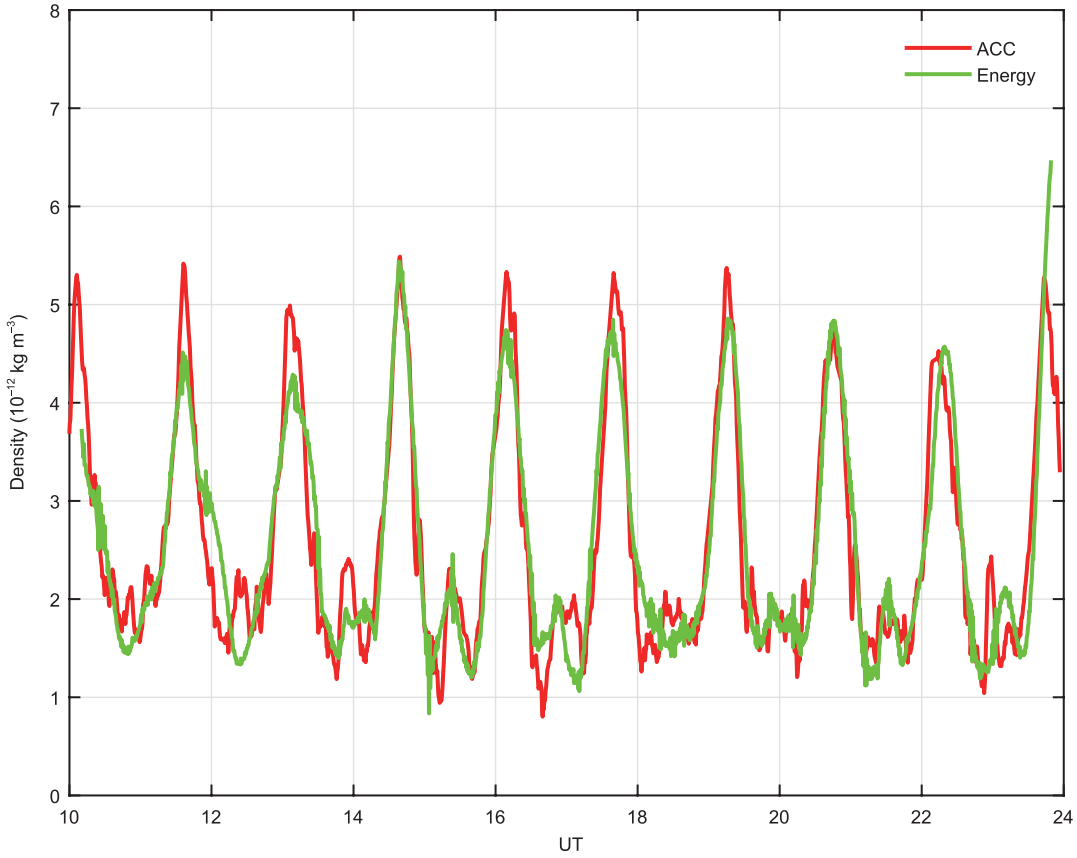

Figure 6 Comparison of densities retrieved from POD data (green) and from accelerometer data (red) on day 32, 2009. Time interval was set to 20 mins.

with those from accelerometer data, as compared with the results shown in Figure 4.

We also compared thermospheric densities from the POD-based energy balance method with those from accelerometer data during 2007–2009. Figure 7a, d and g shows the dependence of the correlation coefficient on thermospheric densities from POD data based on the energy balance method and those from accelerometer data with Δt in 2007, 2008 and 2009, respectively. The blue line represents the annual average daily correlation coefficient, and the red line shows the correlation coefficient for the full-year dataset. The correlation coefficients increased with Δt when Δt was < 25 minutes. Next, Δt=20 minutes was used to derive density from POD data. Both the statistical histograms of the ratio between densities derived from POD data and those from accelerometer data (Figure 7b, e, and h), and corresponding distribution maps of those two densities (Figure 7c, f, and i), show no systematic deviation between densities from POD data and those from accelerometer data. That is, thermospheric densities from these two methods are consistent in a statistical sense. The standard deviations shown in Figure 7b, e, and h decreased over the years 2007 through 2009, at 0.33, 0.27 and 0.21, respectively. In Figure 7, densities derived from accelerometer data are slightly lower than those from POD data, especially under lower thermospheric density. This could be associated with the calibration error of accelerometer data at night when atmospheric density is relatively low, as discussed later.

We also compared the retrieved thermospheric densities from POD and accelerometer data with those from the MSIS00 model. As seen in Figure 8, thermospheric densities calculated from MSIS00 are lower than those derived from POD or accelerometer data, by 20%. Because accelerometer data are calibrated by POD data, thermospheric densities from POD data do not show systematic deviation with respect to those from accelerometer data, although standard deviation of the ratio is larger.

The accuracies of derived thermospheric mass density from POD and accelerometer data are both dependent on the energy decay rate, so the accuracy improves when thermospheric density is high and consequently the decay rate is greater. Therefore, the accuracy of thermospheric density retrieval, especially from POD data, may be associated not only with satellite altitude but also local time. The results in Figure 9 were used to demonstrate local time dependence of the accuracy of derived thermospheric mass density from POD data. As shown in the figure, correlation coefficients between densities retrieved from POD data and those from accelerometer data are relatively large on the dayside, but they become low at night. As mentioned previously, because

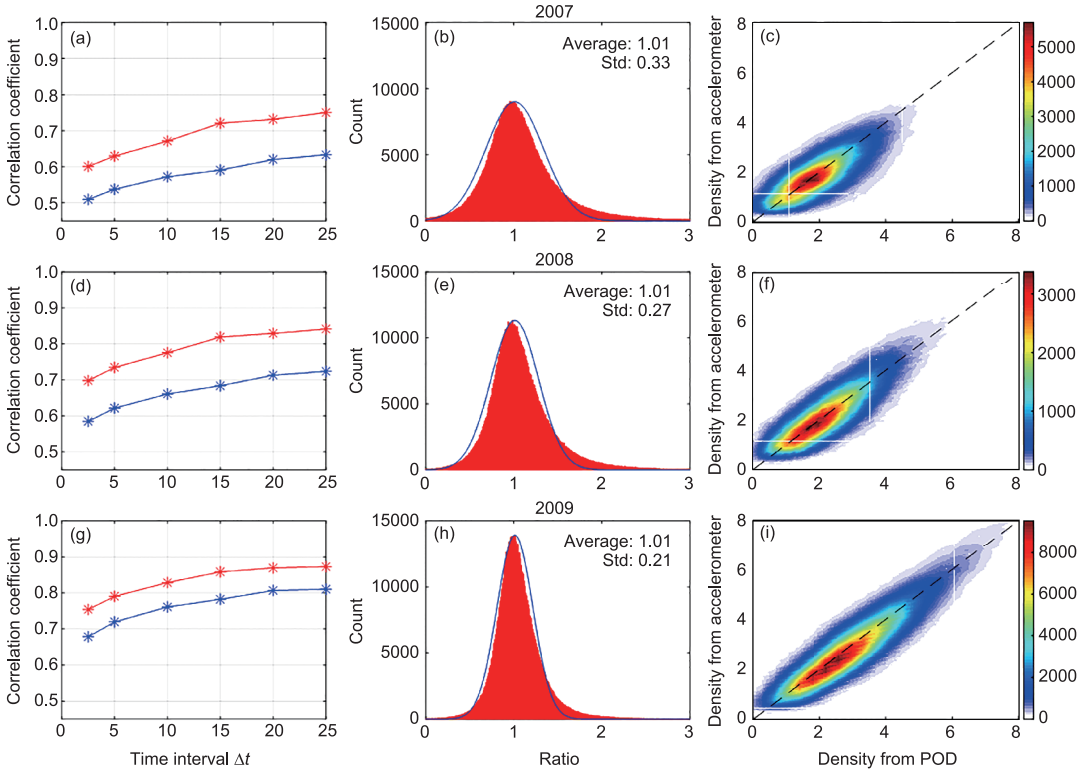

Figure 7 Variation of correlation coefficient between thermospheric densities from POD data and those from accelerometer data as a function of time interval; histograms of ratio between thermospheric densities from POD data and those from accelerometer data and their normal fitting; and corresponding distribution maps in 2007, 2008 and 2009 from top to bottom (density unit: 10^{-12} kg m^{-3}).

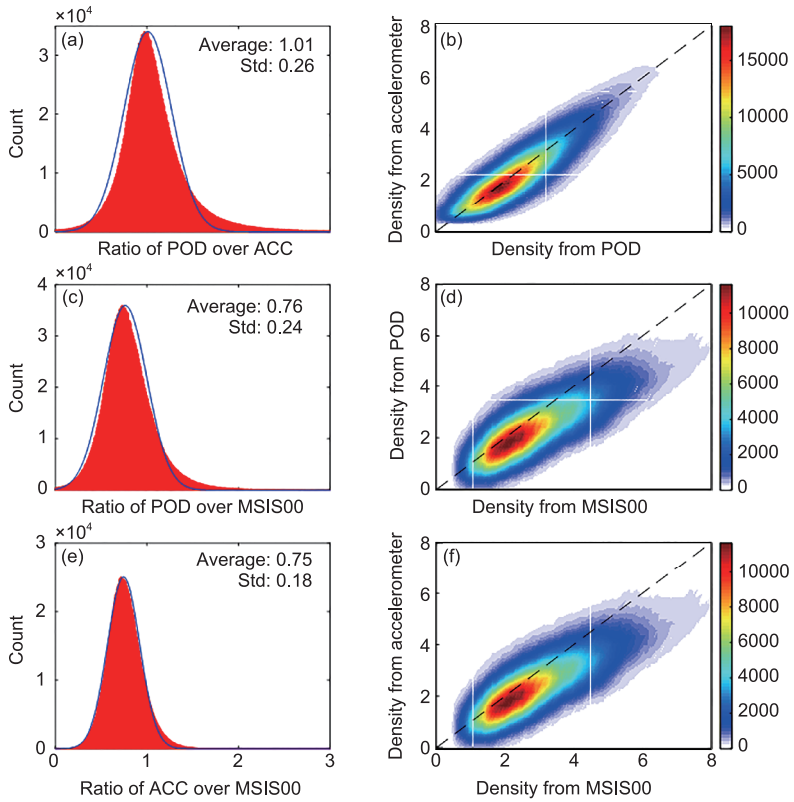

Figure 8 Histogram of ratio between two types of densities among three (from POD data, accelerometer data and MSIS00), and corresponding distribution maps for 2007–2009 (density unit: 10^{-12} kg m^{-3}).

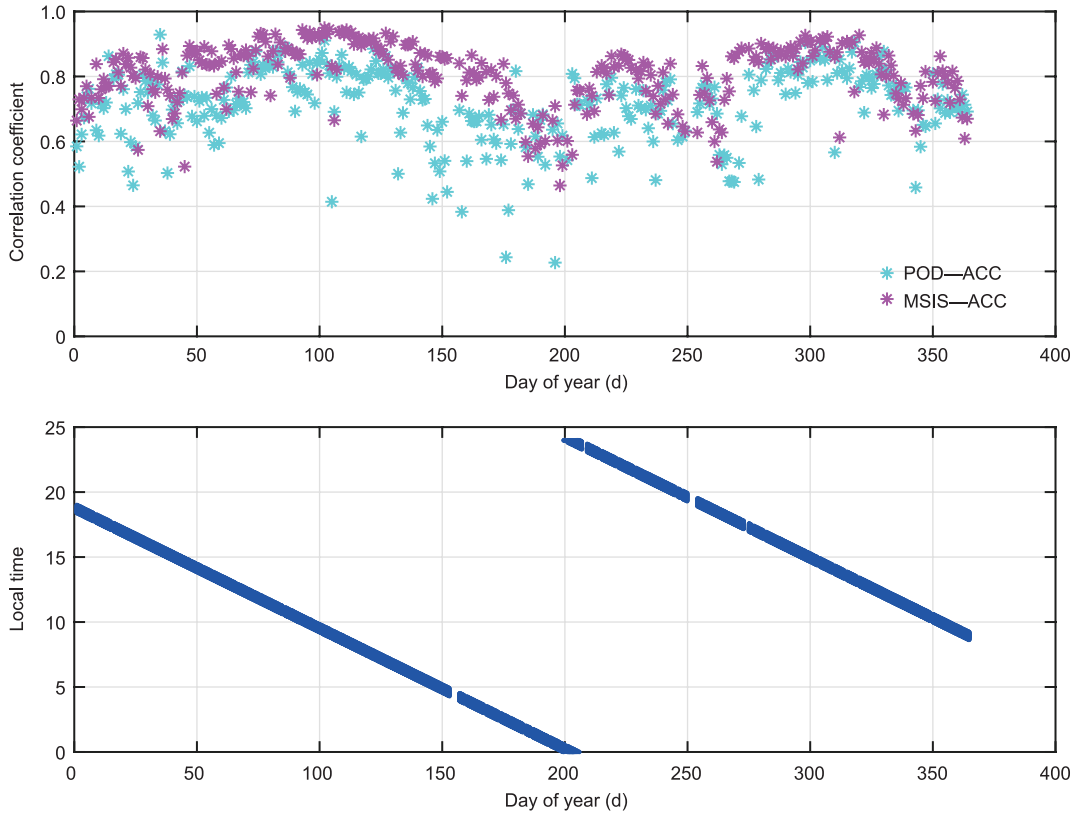

Figure 9 Correlation coefficients between densities retrieved from accelerometer data and those from POD data or MSIS00 in 2009. Local time across the equator is shown in bottom panel. Ascending orbital data are plotted in top panel.

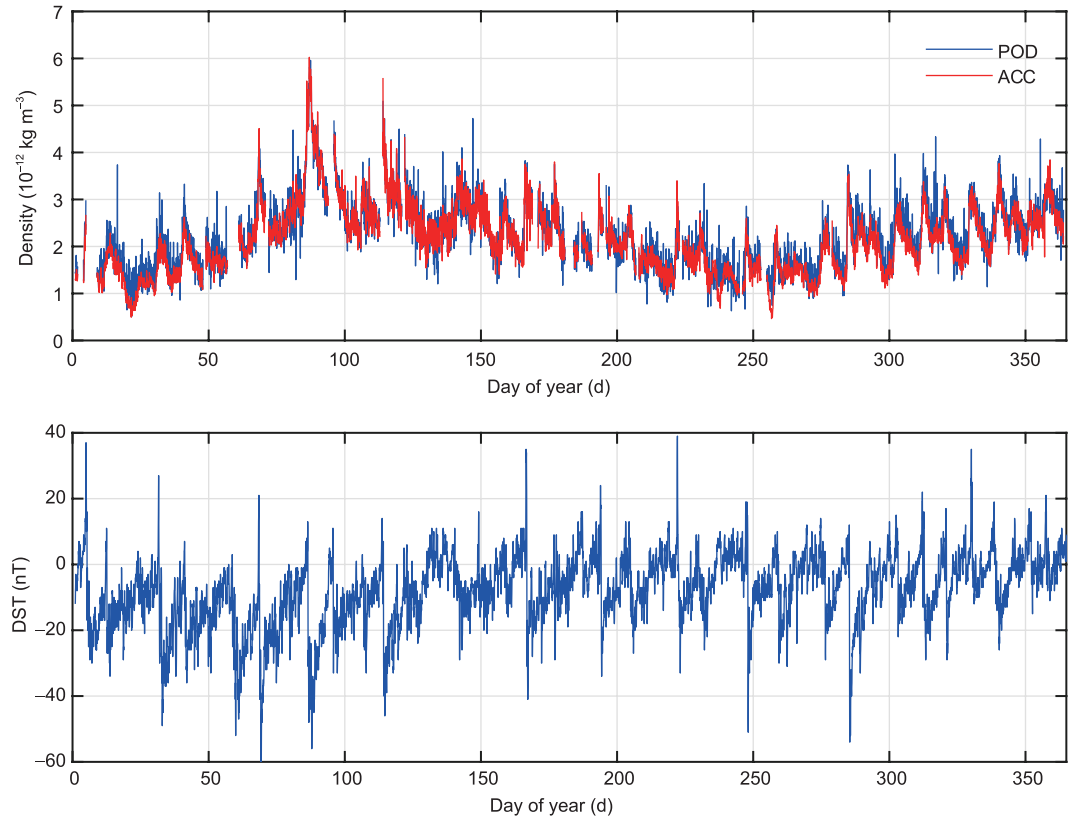

Figure 10 Variation of orbit-average densities and Dst index in 2008. Ascending orbital data are plotted in top panel.

density on the dayside is relatively high because of solar radiation, the resultant energy decay rate is higher, leading to greater retrieval precision of thermospheric density from POD data.

The density derived from POD data can be used to study thermospheric response to geomagnetic activity. As seen in Figure 10, thermospheric mass densities derived from both POD and accelerometer data show a consistent response to geomagnetic activity, as indicated by the Dst index. Thermospheric densities show a clear increase in response to enhanced geomagnetic activity. In addition to long periodic density variations associated with local time and seasonal change, thermospheric densities exhibit strong short-period oscillations with periods of multiple days. Lei et al. (2011b) suggested that these multi-day oscillations in thermospheric density, which are in phase with geomagnetic activity variations, are caused by corotating interaction regions.

5. Summary

In this study, thermospheric densities derived from CHAMP satellite POD data were compared with those from accelerometer data and those calculated from an empirical model for 2007–2009. The major findings are summarized as follows.

(1) Thermospheric mass densities obtained from the semi-major axis decay and energy balance methods are consistent, but computational time for the POD-based density retrieval using the energy balance method is much less.

(2) The uncertainty in retrieved density becomes large when the integration Δt is short, because the accumulated atmospheric drag effect is small. Our analysis indicates that the optimal Δt for CHAMP POD density retrieval is ~20 minutes.

(3) The energy balance method can also be used to calibrate the accelerometer data. Our results show that the calibrated accelerometer data can be used to retrieve thermospheric density with high accuracy.

(4) The accuracy of thermospheric density retrieval from POD data is associated with satellite altitude and local time, and becomes higher when the satellite is at lower altitudes and on the dayside.

Acknowledgements *We thank Dr. Sutton for providing data and helpful discussion, and Mr. Tang Geshi for useful suggestions. This work was supported by the National Natural Science Foundation of China (Grant Nos. 41325017 & 41274158).*

References

Berger C, Biancale R, Barlier F, Ill M. 1998. Improvement of the empirical thermospheric model DTM: DTM94—A comparative review of various temporal variations and prospects in space geodesy applications. J Geodesy, 72: 161–178

Bowman B R, Tobiska W K, Marcos F A, Huang C, Lin C, Burke W. 2008. A new empirical thermospheric density model JB2008 using new solar and geomagnetic indices. In: AIAA/AAS Astrodynamics Specialist Conference, and Exhibit, Guidance, Navigation, and Control and Co-located Conferences. Honolulu. 6438

Bruinsma S, Biancale R. 2003. Total density retrieval with STAR. In: First CHAMP Mission Results for Gravity, Magnetic and Atmospheric Studies. Berlin: Springer. 193–199

Bruinsma S, Tamagnan D, Biancale R. 2004. Atmospheric densities derived from CHAMP/STAR accelerometer observations. Planet Space Sci, 52: 297–312

Calabia A, Jin S. 2016. Assessment of conservative force models from GRACE accelerometers and precise orbit determination. Aerospace Sci Tech, 49: 80–87

Doornbos E, Förster M, Fritsche B, van Helleputte T, van den Ijssel J, Koppenwallner G, Lühr H, Rees D, Visser P, Kern M. 2009. Air density models derived from multi-satellite drag observations. In: Proceedings of ESAs Second Swarm International Science Meeting. Potsdam. 24–26

Doornbos E. 2012. Thermospheric Density and Wind Determination from Satellite Dynamics. Berlin: Springer Science & Business Media

Emmert J T. 2015. Thermospheric mass density: A review. Adv Space Res, 56: 773–824

Flury J, Bettadpur S, Tapley B D. 2008. Precise accelerometry onboard the GRACE gravity field satellite mission. Adv Space Res, 42: 1414–1423

Förste C, Schwintzer P, Reigber C. 2002. Format description: The CHAMP data format. CH-GFZ-FD-001

Hedin A E. 1987. MSIS-86 thermospheric model. J Geophys Res, 92: 4649–4662

Jekeli C. 1999. The determination of gravitational potential differences from satellite-to-satellite tracking. Celestial Mech Dynamical Astron, 75: 85–101

König R, Schwintzer P, Reigber C. 2001. Format description: The CHAMP data format. CH-GFZ-FD-002

Lei J, Thayer J P, Lu G, Burns A G, Wang W, Sutton E K, Emery B A. 2011a. Rapid recovery of thermosphere density during the October 2003 geomagnetic storms. J Geophys Res, 116: A03306

Lei J, Thayer J P, Wang W, McPherron R L. 2011b. Impact of CIR storms on thermosphere density variability during the Solar minimum of 2008. Sol Phys, 274: 427–437

Lei J, Burns A G, Thayer J P, Wang W, Mlynczak M G, Hunt L A, Dou X, Sutton E. 2012. Overcooling in the upper thermosphere during the recovery phase of the 2003 October storms. J Geophys Res, 117: A03314

Li J S. 1995. Satellite Precision Orbit Determination (in Chinese). Beijing: PLA Press. 100–120

Li W W, Li M, Shi C, Zhao L Q. 2016. Thermosphere mass density derivation using on-board accelerometer observations from GRACE satellites (in Chinese). Chin J Geophys, 59: 3159–3174

Liu L. 1992. Orbital Mechanics of Artificial Earth Satellites. Beijing: Higher Education Publication House. 84–99

Lühr H, Grunwaldt L, Förste C, Schwintzer P, Reigber C. 2001. CHAMP reference systems, transformations and standards. Internal publication. GFZ Potsdam. CH-GFZ-RS-002

Marcos F A. 1990. Accuracy of atmospheric drag models at low satellite altitudes. Adv Space Res, 10: 417–422

Michalak G, Baustert G, König R, Reigber C. 2003. CHAMP Rapid Science Orbit Determination—Status and Future Prospects. In: First CHAMP Mission Results for Gravity, Magnetic and Atmospheric Studies. Berlin: Springer. 98–103

Pavlis N K, Holmes S A, Kenyon S C, Factor J K. 2008. An earth gravitational model to degree 2160: EGM2008. EGU General Assembly. 13–18

Petit G, Luzum B. 2010. IERS conventions (2010). IERS Technical Note 36. Frankfurt am Main: Verlag des Bundesamts für Kartographie und Geodäsie.

Picone J M, Emmert J T, Lean J L. 2005. Thermospheric densities derived from spacecraft orbits: Accurate processing of two-line element sets. J Geophys Res, 110: A03301

Picone J M, Hedin A E, Drob D P, Aikin A C. 2002. NRLMSISE-00 empirical model of the atmosphere: Statistical comparisons and scientific issues. J Geophys Res, 107: SIA 15-1–SIA 15-16

Reigber C, Lühr H, Schwintzer P. 2002. CHAMP mission status. Adv Space Res, 30: 129–134

Sang J, Smith C, Zhang K. 2012. Towards accurate atmospheric mass density determination using precise positional information of space objects. Adv Space Res, 49: 1088–1096

Sentman L H. 1961. Free Molecule Flow Theory and its Application to the Determination of Aerodynamic Forces. Sunnyvale: Lockheed Missiles And Space Co Inc

Sutton E K, Nerem R S, Forbes J M. 2007. Density and winds in the thermosphere deduced from accelerometer data. J Spacecr Rockets, 44: 1210–1219

Tapley B D, Bettadpur S, Watkins M, Reigber C. 2004. The gravity recovery and climate experiment: Mission overview and early results. Geophys Res Lett, 31: L09607

Xiong Y Q, Wang H B, Zhao C Y, Xu X L. 2011. A Rapid and Effective Calibration Method for CHAMP Accelerometer. Prog Astron, 29: 228–237

Xu T, Yang Y. 2004. Calibration for CHAMP accelerometry data based on known Earth gravity field model. Acta Geodaetica Cartogr Sin, 2004, 33: 200–204